Check for updates

Inverse design of triblock Janus spheres for self-assembly of complex structures in the crystallization slot *via* digital alchemy†

Luis Y. Rivera-Rivera, [ID] ‡[a] Timothy C. Moore [ID] ‡[a] and Sharon C. Glotzer [ID] ⋆[ab]

The digital alchemy framework is an extended ensemble simulation technique that incorporates particle attributes as thermodynamic variables, enabling the inverse design of colloidal particles for desired behavior. Here, we extend the digital alchemy framework for the inverse design of patchy spheres that self-assemble into target crystal structures. To constrain the potentials to non-trivial solutions, we conduct digital alchemy simulations with constant second virial coefficient. We optimize the size, range, and strength of patchy interactions in model triblock Janus spheres to self-assemble the 2D kagome and snub square lattices and the 3D pyrochlore lattice, and demonstrate self-assembly of all three target structures with the designed models. The particles designed for the kagome and snub square lattices assemble into high quality clusters of their target structures, while competition from similar polymorphs lower the yield of the pyrochlore assemblies. We find that the alchemically designed potentials do not always match physical intuition, illustrating the ability of the method to find nontrivial solutions to the optimization problem. We identify a window of second virial coefficients that result in self-assembly of the target structures, analogous to the crystallization slot in protein crystallization.

1. Introduction

Patchy particles—colloidal nanoparticles with short-ranged, directional interactions—have been the focus of much experimental, computational, and theoretical research over the past two decades.[1–4] Attractive patches produce directional interactions between particles, which influence local valence and, in turn, self-assembly behavior. Therefore, judicious design of patch patterns is critical to self-assembling target colloidal crystals and other superstructures from patchy particles. For example, particles can be designed that self-assemble into open structures,[5–8] and these patchy interactions are often simpler (*e.g.*, smoother functional form and without an excessive number of wells) to achieve both computationally and experimentally than isotropic but oscillatory pair potentials that also self-assemble open structures.[9–12] New techniques in patchy particle synthesis are making ever more complex patch patterns possible,[13,14] bringing ever closer the promise of patchy particles for colloidal matter on demand. However, the high degree of

tailorability of patchy particles is a double-edged sword. On the one hand, the many possible anisotropy dimensions[15] allow, at least in principle, almost any arbitrary particles to be designed; on the other hand, this enormous design space cannot be systematically studied, and efficient means of exploring this space are needed to design particles with useful assembly behavior.[16] Inverse design methods offer a promising approach by starting with a target structure or behavior and seeking points or regions of the design space that give the desired target. For the self-assembly of patchy particles into colloidal crystal structures, inverse design methods attempt to answer the question "what attributes of the patchy interactions lead to the self-assembly of a target crystal structure?" Generally, these attributes can include the number, size, shape, arrangement, and interaction range of the attractive patches, in addition to the shape of the particle core.

To date, most inverse methods design isotropic pair potentials.[9–11,17–34] Considerably less work has focused on the inverse design of anisotropic energetic interactions, including patchy particles.[35–43] Many of those methods rely on high specificity between patchy interactions, which can result in complicated, or even nonphysical, interaction matrices.[37,44]

The digital alchemy framework (DAF),[45] in contrast, is general and therefore particularly attractive for the inverse design of arbitrary patchy particles. Digital alchemy extends standard statistical mechanical ensembles (*e.g. NVT*, *NPT*, *etc.*...) to

[a] *Department of Chemical Engineering, University of Michigan, Ann Arbor, MI, USA.*
E-mail: sglotzer@umich.edu
[b] *Biointerfaces Institute, University of Michigan, Ann Arbor, MI, USA*
† Electronic supplementary information (ESI) available. See DOI: **https://doi.org/10.1039/d2sm01593e**
‡ These authors contributed equally to this work.

include designable particle attributes. The DAF treats parametrizable anisotropy dimensions or other particle interaction attributes as thermodynamic variables, which therefore relax to and fluctuate about equilibrium values. To date, digital alchemy has been used as an inverse design method for the shape of hard polyhedra[45–49] and for isotropic pair potentials.[33,45,50,51] Particles of arbitrary shape or isotropic interaction potentials, respectively, are initialized in the target crystal structure, and the particle shape or potential parameters are relaxed towards values that minimize the free energy of the system in the target structure.

Here, we extend the DAF to patchy particles. In contrast to the inverse design of hard particle shapes, which lack an energy scale, the inverse design of particles with explicit, patchy interactions that contribute to the potential energy presents a unique challenge for the DAF. The directionality afforded by the patches allows interactions that match the coordination of the crystal structure, but can also lead to a trivial ground state solution by making those "valence" interactions of infinite strength, which will dominate the free energy by making thermal fluctuations irrelevant. Potentials designed in this way do not offer useful guidance for designing self-assembling systems. Therefore, constraints on the possible solutions are needed. Previous work using digital alchemy for the inverse design of isotropic pair potentials used a constraint specific to the form of the pair potential.[33] Here, we take a more general approach. Motivated by the "crystallization slot" observed in the solidification of globular proteins,[52] we constrain the system to have a constant second virial coefficient B_2 during the alchemical simulations; doing so ensures we avoid the trivial solution of optimizing for the ground state while promoting solutions that may be in the sweet spot for crystallization. Owing to the generality of the DAF, sampling alchemical variables that correspond to a constant B_2 constraint is straightforward, allowing us to explore the concept of a colloidal crystallization slot.

The second virial coefficient B_2 is the coefficient of the first order correction to the ideal gas law in the virial expansion of the equation of state.[53] Because of its form, B_2 provides a quantitative measure of pairwise interactions between particles: large, negative (positive) values are indicative of strong net attractive (repulsive) pairwise interactions. For particles with a single axis of rotational symmetry like those that are the focus of the current work, B_2 is defined as[53]

$$B_2 \equiv -\frac{1}{2V}\frac{1}{(4\pi)^2}\int \left[e^{-\beta U} - 1\right] d\mathbf{r}_1 d\mathbf{r}_2 d\mathbf{q}_1 d\mathbf{q}_2, \quad (1)$$

where V is the volume, $\beta \equiv 1/k_B T$ is the inverse temperature, U is the potential energy, and $\mathbf{q}_i$ and $\mathbf{r}_i$ represent the orientational and translational degrees of freedom, respectively, of particle i. We work with the normalized second virial coefficient b_2, defined as $b_2 = B_2/B_2^{HS}$ where $B_2^{HS} = 2\pi\sigma^3/3$ is the second virial coefficient of a system of hard spheres (HS) with diameter σ.

The second virial coefficient is widely used as a predictor of thermodynamic quantities such as the vapor–liquid critical point,[54] and as an extended law of corresponding states for colloidal and protein suspensions,[55,56] is indicative of viscosity in antibody solutions,[57] and most relevant for this work, is a predictor of protein crystallization propensity.[52] George and Wilson[52] were the first to report on the correlation between b_2 and crystallization propensity for aqueous solutions of globular proteins, showing that water soluble, globular proteins crystallize at experimental conditions that yield b_2 values within the relatively narrow range of $-10 \lesssim b_2 \lesssim -1$, named the "crystallization slot". Similar crystallization slots have been uncovered for different groups of proteins,[58–63] and a similar concept has also been proposed for colloidal suspensions,[56,64] but has thus far received far less attention than for protein solutions. Although a system at conditions within the crystallization slot is not guaranteed to crystallize,[62,65,66] nor is crystallization exclusively restricted to conditions within the slot, the crystallization slot concept remains an important guide for exploring the high-dimensional space of parameters that influence crystal yield.

In this work, we leverage the crystallization slot concept and employ b_2 as a constraint in alchemical simulations to design patchy particles that self-assemble target crystal structures using triblock Janus spheres as an example model. Triblock Janus spheres are particles whose surfaces contain three distinct regions of different chemical coatings, resulting in orientation-dependent interparticle interactions.[67] Experimentally, triblock Janus particles are often synthesized to have hard-sphere-like interactions between equatorial bands and attractive interactions between polar regions of the particles, which can be either symmetric or asymmetric in size and location on the particle surface.[5,67]

The rest of the paper is organized as follows: in Section 2, we describe the particle model that we employ and the implementation of the b_2-constrained digital alchemy-based inverse design method to optimize the interactions of the particle model for the self-assembly of selected crystal structures. In Section 3, we present the designed particle interactions and self-assembly results for three distinct crystal structures: the kagome and snub square lattices in two dimensions, and the pyrochlore lattice in three dimensions. Finally, in section 4, we conclude with suggestions for future work.

2. Model and methods

2.1 Triblock Janus sphere model

We model triblock Janus spheres using the Kern–Frenkel (KF) potential,[68] illustrated in Fig. 1. Particles have a hard sphere of
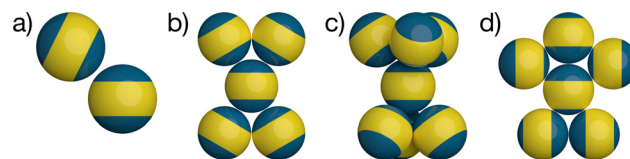

Fig. 1 (a) Triblock Janus spheres interacting *via* the Kern–Frenkel potential. Particles within the range of interaction ($\sigma < |\mathbf{r}_{ij}| \leq \lambda\sigma$) interact only if the patches are facing each other (*i.e.*, if the vector joining the center of the particles intersects both patches, as in (a). (b and c) Kagome and pyrochlore motifs formed by triblock Janus spheres with symmetric patches in 2D and 3D, respectively. (d) The snub square motif, which contains an asymmetric valence around each particle, suggesting a need for patches of unequal size.

diameter σ with an attractive, circular patch on each pole. The location of patch k on particle i is denoted by an orientational director $\mathbf{n}_i^k$ that extends from the center of the particle to the center of the patch, where $k \in \{1, 2\}$ for the triblock Janus particles studied in this work. Patch sizes are quantified by an aperture angle θ_i^k so the total opening angle of each patch is $2\theta_i^k$. In general, the patches need not be the same size.

We denote the position of the center of particle i by $\mathbf{r}_i$, and we adhere to the convention that the vector $\mathbf{r}_{ij}$ points from the center of particle i to the center of particle j, giving $\mathbf{r}_{ij} = \mathbf{r}_j - \mathbf{r}_i$, with magnitude $r_{ij} = |\mathbf{r}_{ij}|$, and unit vector $\hat{\mathbf{r}}_{ij} = \mathbf{r}_{ij}/r_{ij}$. Following these conventions, we write the KF potential as $U^{KF} = U^{SW}(\mathbf{r}_{ij})f(\hat{\mathbf{r}}_{ij}, \mathbf{n}_i^l, \mathbf{n}_j^m)$. The first factor is the isotropic square-well (SW) potential that depends only on the distance between the particles and is given by

$$U^{SW}(r) = \begin{cases} \infty & r \leq \sigma \\ -\beta\varepsilon & \sigma < r \leq \lambda\sigma \\ 0 & \text{otherwise} \end{cases} \quad (2)$$

where $\beta = 1/k_B T$ with k_B the Boltzmann constant and T the temperature, ε is the well depth corresponding to the strength of the interaction and λ is the range of the interaction, related to the width of the well δ by $\lambda \equiv 1 + \delta/\sigma$. The parameters ε and σ set the energy and length scales in our simulations. The anisotropy of the pair potential is accounted for via the orientational masking function f, defined as

$$f(\hat{\mathbf{r}}_{ij}, \mathbf{n}_i^l, \mathbf{n}_j^m) = \begin{cases} 1 & \text{patches aligned} \\ 0 & \text{otherwise} \end{cases} \quad (3)$$

where the patch alignment condition is $\hat{\mathbf{r}}_{ij}\cdot\mathbf{n}_i^l > \cos(\theta^l) \wedge \hat{\mathbf{r}}_{ji}\cdot\mathbf{n}_j^m > \cos(\theta^m)$ for any patch l on particle i and any patch m on particle j. The simplicity of the KF model makes it amenable to theoretical treatment, including an analytical solution to eqn (1) that results in

$$b_2(\chi,\lambda,\varepsilon) \equiv \frac{B_2^{KF}(\chi,\lambda,\varepsilon,\sigma)}{B_2^{HS}(\sigma)} = 1 - \chi^2(\lambda^3 - 1)(e^{+\beta\varepsilon} - 1) \quad (4)$$

where $\chi = \chi_1 + \chi_2$ is the total fraction of surface covered by all the patches and $\chi_k = \sin^2(\theta^k/2)$ is the contribution of each patch with aperture angle θ^k.

We treat the interaction potential attributes $\alpha = (\chi,\lambda,\varepsilon)$ as alchemical variables. These alchemical variables have conjugate alchemical potentials, $\mu(\alpha)$, that encode the system's response to changes in the alchemical variables. The alchemical variables are allowed to fluctuate subject to the constraint $b_2(\chi,\lambda,\varepsilon) = b_2^0$, a predefined constant. This scheme defines a holonomic constraint on the surface of constant b_2 of the form $\Phi(\chi,\lambda,\varepsilon) = b_2(\chi,\lambda,\varepsilon) - b_2^0 = 0$. In the next section we describe our simulation protocol and how we enforce this constraint.

2.2 Implementation of digital alchemy for patchy interactions and simulation protocol

We implemented the alchemical Monte Carlo (MC) method within the hard particle MC (HPMC) module of the HOOMD-blue simulation engine[69,70] and used the runtime-compiled

code to compute the energetic interactions defined in eqn (2) and (3). We performed one alchemical trial move for each conventional translational and rotational MC move. Alchemical trial moves consist of proposing a randomly selected displacement on Φ from α_1 to α_2. To do this we implemented a variation of the surface diffusion algorithm described elsewhere,[71] with the surface $\Phi(\chi,\lambda,\varepsilon) = 0$ defined above, and with the distinction that we impose additional constraints on the extrema of α motivated by geometrical considerations. Specifically, we set $\lambda_{min} = 1.01$ and $\lambda_{max} = 2$, and $\chi_{min} = 0.001$ and $\chi_{max} = 0.8264$, which correspond to $\theta_{min} \approx 2.5°$ and $\theta_{max} \approx 80°$. The chosen range of λ spans interactions extending over very short distances to distances well beyond the first neighbor shell of most structures and densities of interest. Similarly, the chosen range of θ allows the formation of multiple bonds per patch commensurate with the valence of the target structures, while avoiding overlap between patches on the same particle. We automatically rejected trial moves that resulted in a value of α outside of these limits. Otherwise, moves were accepted or rejected based on a generalized Metropolis criterion, $P_{1\to2} = \min\{1, e^{-\beta(U(\alpha_2) - U(\alpha_1))}\}$. We tuned the sizes of the translational, rotational, and alchemical steps to achieve an acceptance probability of ~40%.

We chose target b_2^0 values in the range $-40 \leq b_2^0 \leq 0$, which spans the colloidal crystallization slot we identified in the literature, but also extends to more negative values to test the validity of the colloidal crystallization slot. For each b_2^0, we ran 120 independent alchemical simulations with different initial α on a roughly uniform grid. We placed the particles in an external harmonic field that restrains their positions and orientations to the ideal Einstein crystal for the first few steps of a run. This initial setup allows the alchemical degrees of freedom to relax towards values that are optimal for the target structure before the structure has a chance to fall apart. We ran the optimization simulations for 500×10^3 total MC sweeps, linearly decreasing the strength of the harmonic field to zero over the first 200×10^3 steps. We ran the final 300×10^3 MC sweeps without the harmonic restraints, but b_2^0 always remained constant.

We labeled each optimization run as successful or failed based on the stability of the target structure as follows. We first used the EnvironmentMotifMatch module of the freud analysis library[72] to determine which particles have a local coordination that is similar to that in the target structure.[73] We used a threshold of 0.2 for the environment matching calculation, chosen via visual inspection. We labeled a run as successful if at least 90% of the particles remained in environments that resemble the target structure, and failed otherwise.

We also used EnvironmentMotifMatch to analyze the self-assembled structures by quantifying the fraction of particles Υ that have local environments that resemble the target structure: $\Upsilon = N_{match}/N_{total}$ where N_{match} is the number of particles with a local coordination similar to that of the target structure and N_{total} is the total number of particles in the system. We note that because the particles self-assemble into finite crystallites, particles at the boundary are undercoordinated relative to the reference motifs used in the EnvironmentMotifMatch analysis, and therefore do not register as crystal-like, lowering Υ.

In the next section we present DAF-designed particles obtained from the b_2-constrained alchemical MC optimization scheme applied to triblock Janus spheres to assemble kagome, pyrochlore and snub square structures. We validate the resulting designs by performing self-assembly simulations and observing assembly from the fluid into the target structures. The self-assembly simulations were performed using MC but without any alchemical moves.

3. Results and discussion

3.1 Kagome design: triblock Janus spheres in 2D

We designed kagome structures at crystal phase densities (*i.e.*, area or volume fraction in 2D and 3D, respectively) of $\phi_{target} \in \{0.5, 0.6\}$. At these densities, the minimum interaction range required to form a bond between particles in the first coordination shell is $\lambda \approx 1.0647$ and $\lambda = 1.166$, respectively. These λ values also correspond to the locations of the first peak in the radial distribution function (RDF) in the ideal crystal at those densities. We began by placing 507 particles in the ideal kagome lattice at the target density and followed the protocol described in the previous section.

Fig. 2a shows the alchemical optimization paths of a subset of the 120 initial points (black crosses) in alchemical space distributed on a roughly uniform grid of the $b_2^0 = -4$ surface, at $\phi_{target} = 0.6$. Out of the 120 initial points, 87 (72.5%) meet the success criterion at the end of the simulations. Successful optimization paths are indicated by solid lines while dashed lines indicate simulations where the optimization algorithm

failed to obtain a solution within the desired design space (*e.g.*, the initial target structure melted partially or completely or transitioned into a hexagonal lattice). Most of the failed optimization paths end on, or close to, the extrema boundaries imposed on the alchemical variables.

All successful paths converge to the single point $\alpha = (37°, 1.12, 5.8)$, which we deem the optimal parameters $\alpha*$ and denote with a star in Fig. 2a. In contrast, previous inverse design work using digital alchemy to optimize isotropic pair potentials found multiple solutions for a given target crystal structure.[33] We obtained $\alpha*$ by computing the "time" average of each patch parameter over the final 100×10^3 MC steps and then averaging all individual time averages across all successful runs. Notably, this combination of $(\theta*, \lambda*)$ corresponding to $\alpha*$ is well within the range of the two-bond-per-patch condition given by $(2\lambda)^{-1} \leq \sin\theta < \sqrt{3}(2\lambda)^{-1}$ arising from purely geometrical considerations (see Fig. S3, ESI†). This result showcases the ability of our approach to produce results that are consistent with intuition in simple cases. In addition, the width of the optimal interaction range $\delta*/\sigma = \lambda* - 1 = 0.12$ is approximately twice as large as the minimum interaction width required to form a bond between particles in the first coordination shell, $\delta/\sigma \approx 0.0647$. This result is consistent with the fact that the KF potential is a square-well potential, and therefore the vibrational entropy is maximized when all particles are in the middle of the interaction range of their neighbors.[74]

Fig. 2c shows a summary of the optimal alchemical parameters for triblock Janus spheres in a kagome lattice as a function of b_2^0 and ϕ_{target}. From this figure we see that the
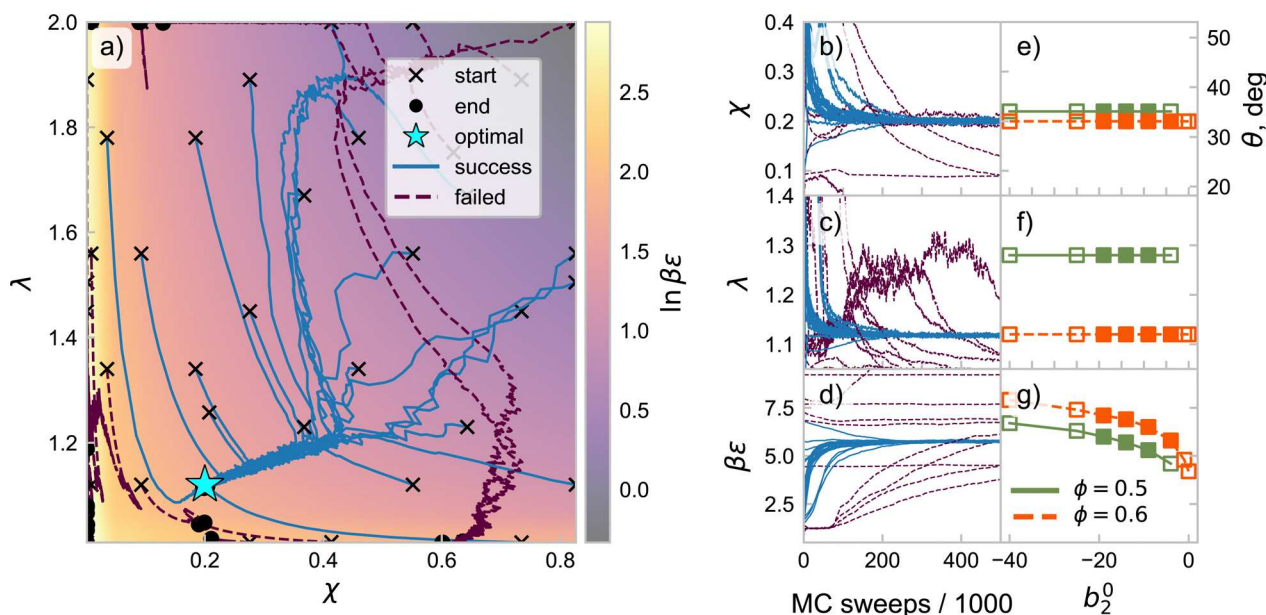

Fig. 2 Patch alchemy results for the kagome lattice. (a) The surface of constant $b_2^0 = -4$, showing the initial (black crosses) and final (black dots) alchemical simulation points and the paths between them on the design space. For clarity, only 25% of the initial points are displayed. Paths that yield stable kagome lattices are labeled "success" and those that don't are labeled "failed". (b–d) The evolution of the alchemical parameters during the optimizations for systems with $b_2^0 = -4$ at $\phi = 0.6$, colored the same as (a). (e–g) The optimized values of the alchemical parameters as a function of b_2^0 and ϕ after identifying stable clusters on the b_2 surface. Filled markers indicate optimized solutions with $\Upsilon \geq 50\%$ (see Model and methods) in self-assembly simulations.

optimal patch aperture angle θ and interaction range λ remain constant with b_2^0 for a given ϕ_{target}, while ε increases as b_2^0 becomes more negative. The target density has a negligible effect on θ since θ is mostly controlled by the valence of the target structure. The largest effect of ϕ_{target} is on the interaction range λ, which is expected for the KF potential since it is this interaction range that ultimately determines the lattice constant of the resulting crystal and therefore its crystal phase density. At $\phi_{target} = 0.5$, the width of the optimized potential with $\lambda^* = 1.28$ ($\delta = 0.28$) is approximately 1.7 times that of the minimum potential required to form bonds in the ideal crystal at the same density, which is consistent with the aforementioned design rule and entropy maximization principle.

To validate our alchemy results, we performed three independent self-assembly simulation replicas for all the combinations of (b_2^0, ϕ_{target}) for which we successfully obtained optimal values of $(\theta^*, \lambda^*, \varepsilon^*)$. We started each simulation with a random configuration of $N = 1200$ particles at an area fraction of $\phi = 0.3$. We chose more dilute systems for assembly compared to the optimization simulations (i.e., the density of the optimization simulations was the target crystal density ϕ_{target}) to minimize the effect of the periodic boundary conditions used in the assembly simulations. Because systems of the inversely designed particles have negative b_2 values, they will spontaneously aggregate without an external pressure and can therefore form finite aggregates that do not span the simulation box. As indicated in Fig. 2e–g, we find an increased assembly propensity (defined as systems where $\geq 50\%$ of particles form kagome-like local environments) for $-20 \leq b_2^0 \leq -5$, qualitatively analogous to the crystallization slot identified in the protein crystallization community.

Fig. 3 shows the self-assembly results corresponding to the design parameters obtained from the alchemical simulations shown in Fig. 2a–d (e.g., $b_2^0 = -4$ and $\phi_{target} = 0.6$). Fig. 3a shows the final snapshot of one of the replicas; visual inspection clearly reveals that the local environment of most particles matches the typical X-like motif of the kagome lattice (Fig. 1b). Fig. 3b shows the evolution of the intensive potential energy $\beta U/N$ and crystal yield Υ (see Model and methods). We observed a crystal yield of $\Upsilon \approx 85\%$ in all three replicas.

We further characterized the final structures by computing the RDFs, shown in Fig. 3c. The vertical dashed black lines correspond to the peak locations of the ideal kagome lattice at $\phi = 0.6$. The radial axis is normalized by the location of the first peak in the RDF for the potential optimized at $\phi_{target} = 0.6$, which is $r_0 \approx 1.056$ in this particular case. Note that this value roughly corresponds to the midpoint of the width of the potential $(1 + \lambda)/2 = 1.06$ and is in good agreement with the location of the first peak of the RDF of the ideal lattice, at the same density as discussed above. Moreover, we highlight the fact that the RDFs of the systems simulated with the model optimized at $\phi_{target} = 0.5$ have peaks whose locations are scaled in the r-direction by a factor of appproximately $\sqrt{0.6/0.5} \approx 1.1$. Hence, the self-assembled crystals seem to locally adopt ϕ_{target}, even at much more dilute state points, and ϕ_{target} therefore serves as a handle to control the lattice spacing of the self-assembled crystals.
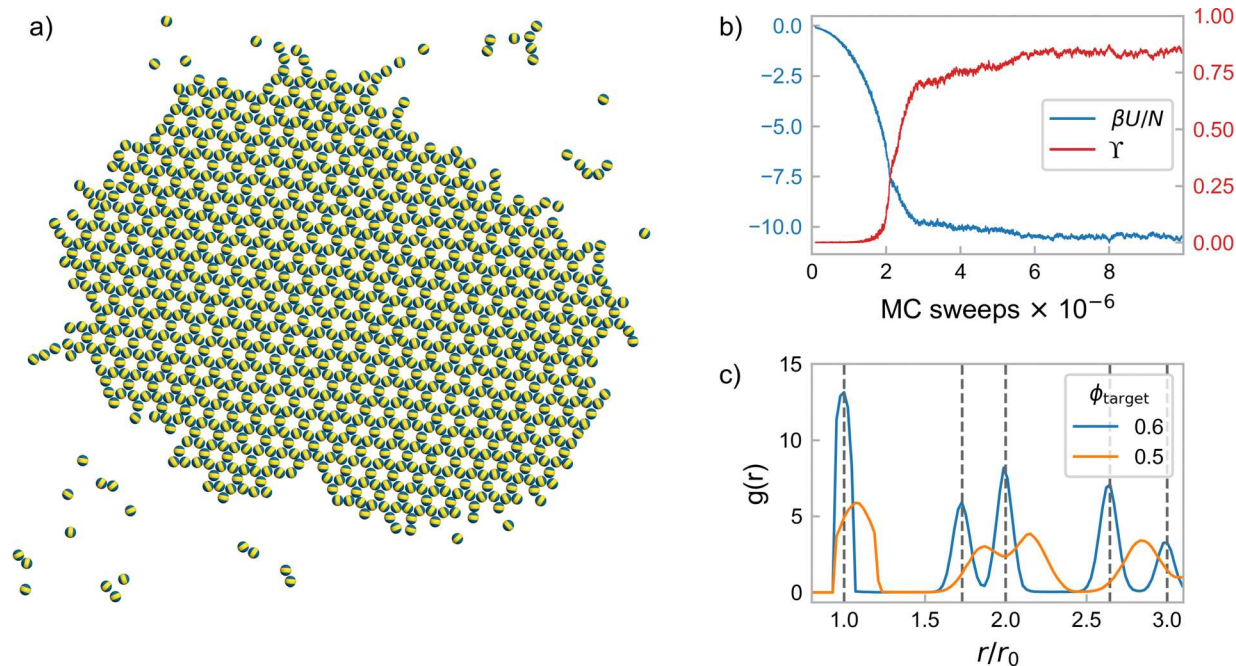
Fig. 3 Self-assembly results for the kagome lattice with $\alpha^* = (37°, 1.12, 5.8)$ obtained from alchemical simulations at $b_2^0 = -4$ and $\phi_{target} = 0.60$ (Fig. 2a). (a) Snapshot of the last simulation frame showing the self-assembled kagome lattice. (b) Progression of the intensive potential energy $\beta U/N$ and crystal yield Υ (see Model and methods). (c) RDFs of the assembled kagome structures for $(b_2^0, \phi_{target}) = (-4, 0.6)$ and $(-9, 0.5)$; the vertical dashed lines represent the RDF of the ideal kagome lattice. In all cases, the radial axis is normalized by the location of the first peak of the assembled structure at $\phi_{target} = 0.6$, given by $r_0 \approx 1.056$. The relative locations of the peaks in the assembled structure are in very good agreement with those of the ideal crystal. The RDFs were computed over the final 2×10^6 MC sweeps of the assembly simulations.

3.2 Pyrochlore design: triblock Janus particles in 3D

We next apply the b_2-constrained digital alchemy methodology to design a colloidal system to self-assemble a pyrochlore lattice at crystal densities of $\phi_{\text{target}} = 0.25$ and $\phi_{\text{target}} = 0.35$. In this case we initialized 432 particles in the ideal pyrochlore structure and followed the same protocol as for kagome. The colloidal pyrochlore (or cubic tetrastack) crystal is one of the few 3D structures known to have a complete photonic band gap and is also a stable phase of triblock Janus particles interacting via the KF potential.[74] Fig. 4a shows a subset of the alchemical optimization paths for $b_2^0 = -9$ and $\phi_{\text{target}} = 0.34$. Unlike for the kagome structure where we observed a single optimal point on the b_2 surface, here we observe two candidate optimal points on the b_2 surface: $\alpha_1 = (44°, 1.06, 6.6)$ and $\alpha_2 = (68°, 1.85, 1.7)$ with 60 and 14 converging paths, respectively. The former candidate optimal design point is well within the range of values of previously studied KF phase diagrams.[8,74] Although the available phase diagrams of triblock Janus spheres do not extend enough to include the latter point,[8,74] it can be unambiguously located in the fluid region of these by a simple visual interpolation. Furthermore, self-assembly simulations confirm this conclusion (i.e., no stable clusters form in assembly simulations using patchy interactions corresponding to α_2). Therefore, pyrochlore is a metastable phase for the system at α_2, and we discard α_2 as a solution to the optimization problem.

Contrary to the kagome case study, where the (θ^*, λ^*) combination allowed a maximum number of bonds that is commensurate with the valence of the structure, the combination of (θ^*, λ^*) obtained in the pyrochlore optimization is slightly above the four-bonds-per-patch lower limit, despite the coordination of the lattice containing three bonds per patch.

In the next section we explore the implications of this counterintuitive result. The width of the optimal interaction range $\delta^*/\sigma = \lambda^* - 1 = 0.06$ is approximately twice as large as the minimum interaction width required to form a bond between particles in the first coordination shell at the target ϕ_{target}, $\delta/\sigma \approx 0.0288$, which is in agreement with the kagome results and with the vibrational entropy maximization design rule discussed in the previous section.

Fig. 4e–g shows a summary of the optimal alchemical parameters as a function of b_2^0 and ϕ_{target}. Here, we confirm the design rule trends established in the previous case study. First, we see that the optimal patch aperture angle θ and interaction range λ remain approximately constant with b_2^0 for a given ϕ_{target}, while ε increases as b_2^0 becomes more negative. As before, the target crystal phase density has a negligible effect on θ but has a large effect on the interaction range λ.

As for the kagome lattice, we performed self-assembly simulations for all the combinations of $(b_2^0, \phi_{\text{target}})$ for which we obtained optimal α. We initialized the simulations with random configurations at $\phi = 0.1$ to minimize the effect of pressure on the assembly. Fig. 5 shows the self-assembly results corresponding to the design parameters obtained from the alchemical simulations shown in Fig. 4a and b (e.g., $b_2^0 = -9$ and $\phi_{\text{target}} = 0.34$). Fig. 5a shows a snapshot of a subset of all the particles in the system forming a crystalline grain. In this case, $\Upsilon \approx 43\%$ (Fig. 5b, red line). We attribute the relatively lower value of Υ (compared to the kagome results) to polymorphism, i.e., the presence of a competing structure with a similar free energy to the target pyrochlore lattice. Pyrochlore has a closely related hexagonal polymorph, the hexagonal tetrastack (HT), with identical valence (six neighbors, three above and three below like
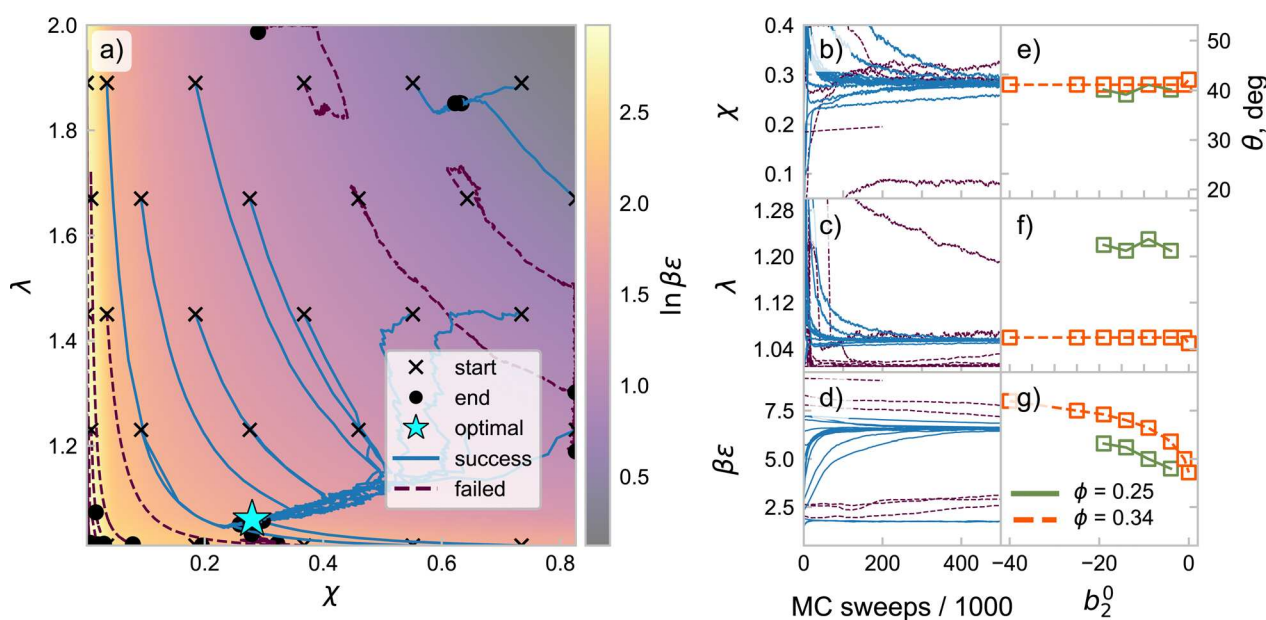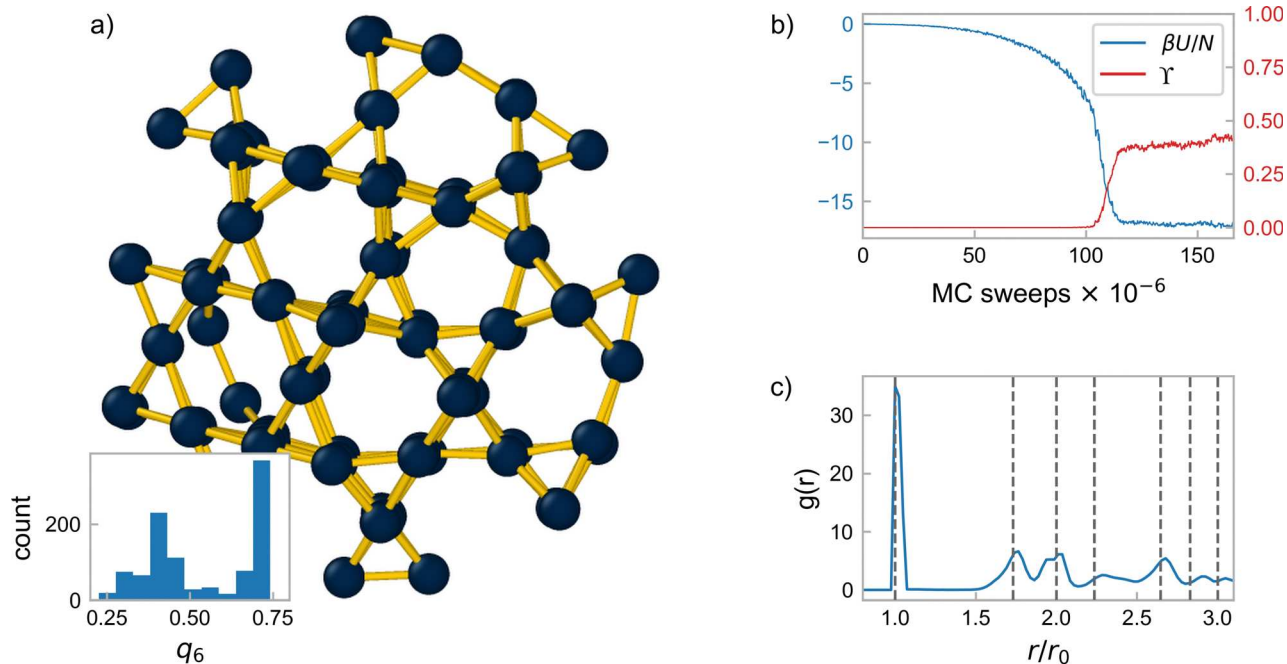

Fig. 4 Patch alchemy results for the pyrochlore lattice. (a) The surface of constant $b_2^0 = -9$, showing initial points as black crosses, final points as black dots, and the path each optimization takes on the surface as lines. Failed optimizations are drawn as dashed lines, while successful optimizations are drawn as solid lines. (b–d) The evolution of the alchemical parameters during optimization, coloring the same as in (a). (e–g) The optimized values of the alchemical parameters as a function of b_2^0. Notice the patch width and range remain nearly constant as a function of b_2^0.

Fig. 5 Self-assembly results for the pyrochlore lattice with $\alpha^* = (44°, 1.06, 6.6)$ obtained from alchemical simulations at $b_2^0 = -9$ and $\phi_{\text{target}} = 0.34$ (Fig. 4a). (a) Snapshot of a crystalline grain showing the assembled pyrochlore lattice. For clarity, patches are not drawn and particle sizes are rendered with a radius of $\sigma/2$. Bonds are drawn between the particles in the first neighbor shell. Inset: Distribution of per-particle Steinhardt bond orientational order parameter q_6 in the final self-assembled configuration. (b) Progression of the intensive potential energy $\beta U/N$ and crystal yield Υ (see Model and methods). The lower value of Υ, as compared to the kagome assembly, is attributed to polymorphism. (c) The radial distribution function of the assembled pyrochlore (blue) compared with the ideal pyrochlore (dashed black lines). The radial axis is normalized by the location of the first peak of the assembled structure, $r_0 \approx 1.013$. The relative locations of the peaks in the assembled structure are in relatively good agreement with those of the ideal crystal.

pyrochlore), but with an "eclipsed" configuration instead of the "staggered" one shown in Fig. 1c. The bimodal distribution of the Steinhardt bond orientational order parameter q_6[75,76] indicates that motifs of both polymorphs are present in the self-assembled crystallite (Fig. 5a, inset). Both the ideal pyrochlore and HT structures exhibit a peak at $q_6 = 0.741$.[77,78] However, the latter exhibits an extra smaller peak at $q_6 = 0.411$.[77,78] The presence of peaks around these values indicates a mixture of the two polymorphs. While the problem of polymorph selection is beyond the scope of the current work, we hypothesize it could be addressed by adding additional alchemical degrees of freedom to allow fluctuations in the patch geometries and arrangement, or by adding repulsive patches that disfavor the unwanted polymorph through negative design.[79] For example, Romano and Sciortino[41] showed how the shape of patches can be made to favor one polymorph over another, so one may imagine making the shape of the patches an alchemical degree of freedom to aid in polymorph selection. Similar considerations arise in designing patchy particles to assemble cubic diamond, where cubic and hexagonal polymorphs often compete with each other.[37,39,40,80]

3.3 Snub square design: triblock Janus spheres with asymmetric patches

The kagome and pyrochlore examples illustrate the design of triblock Janus particles with symmetric patches (equal-size aperture angles) in 2D and 3D, respectively. To demonstrate the applicability of our method to more complex crystal structures, we now relax the equal-size patch constraint to allow both patch sizes to fluctuate individually while still subject to the b_2 constraint. For this purpose, eqn (1) is easily generalized to account for asymmetric patch sizes, resulting in $b_2 = 1 - (\chi_1 + \chi_2)^2(\lambda^3 - 1)(e^{\beta \varepsilon} - 1)$ where $\chi_i = \sin^2(\theta_i/2)$ is the surface fraction covered by each of the patches.

We use this approach to design triblock Janus spheres that minimize the free energy of a snub square lattice at a crystal area fraction of $\phi_{\text{target}} = 0.59$. The snub square lattice has been demonstrated to be a stable phase of soft patchy particle models,[81] binary mixtures of hard patchy polygons,[82] non-additive square-well particles,[83] isotropic interaction potentials in a single component system[9,28] and in several experimental systems.[84–87] This lattice therefore makes an ideal candidate for a stress test of our algorithm, since the neighbors in the coordination shells surrounding each particle have an asymmetric spatial distribution (3 on one pole and 2 on the opposite pole, see Fig. 1d). This asymmetric valence distribution strongly suggests the need for unequal patch sizes on each pole to stabilize the structure. However, the snub square crystal structure is fairly complex, with an 8-particle unit cell and 4 unique particle orientations, so it is unclear *a priori* whether or not it is an equilibrium phase of any triblock Janus sphere model or whether or not such particles can self-assemble into the structure.
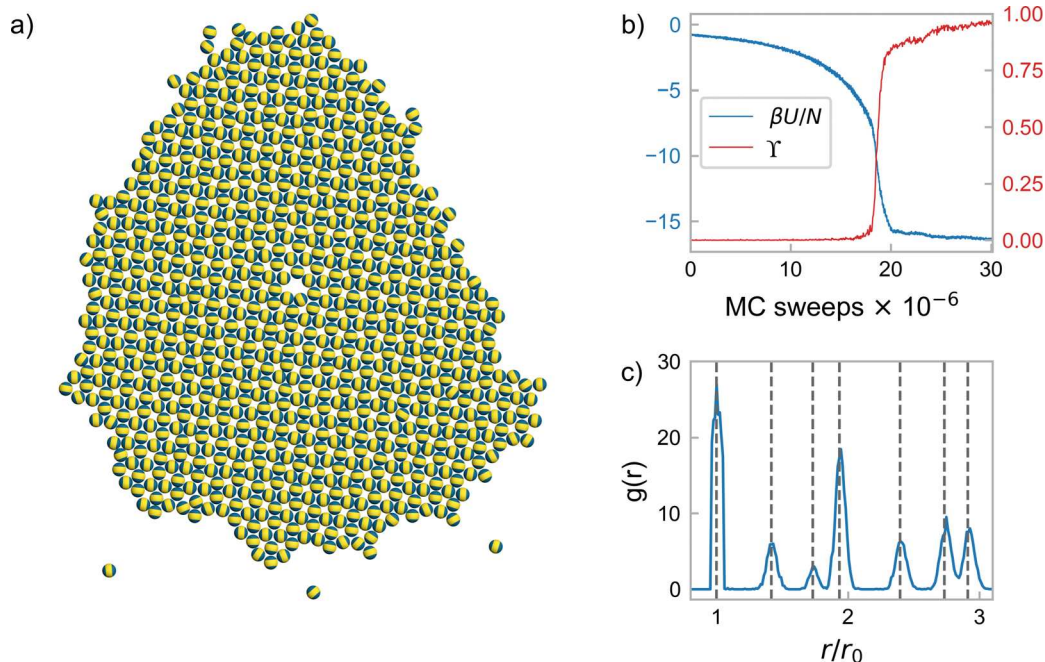
Fig. 6 Self-assembly results for the snub square lattice with $\alpha^* = (67°, 38°, 1.1, 6.0)$ obtained from alchemical simulations at $b_2^0 = -19$ and $\phi_{\text{target}} = 0.59$. (a) Snapshot of the final configuration from the simulation showing the assembled snub square lattice. (b) Progression of the intensive potential energy $\beta U/N$ and crystal yield Υ (see Model and methods), showing a final yield of $\Upsilon \approx 94\%$. (c) The radial distribution function of the assembled snub square (blue) compared with the ideal lattice (dashed black lines). The radial axis is normalized by the location of the first peak of the assembled structure, $r_0 \approx 1.0438$. The relative locations of the peaks in the assembled structure are in very good agreement with those of the ideal crystal.

With the exception of having an additional alchemical degree of freedom, the optimization procedure is equivalent to the one used in the kagome and pyrochlore case studies. We performed the optimizations for systems of 512 particles at $b_2^0 = -19$, within the colloidal crystallization slot. The extended set of optimal parameters α^* obtained from alchemical simulations in this case are $\theta_L^* \approx 67°$, $\theta_s^* \approx 38°$, $\lambda^* \approx 1.10$ and $\varepsilon^* \approx 6.0$, where subscripts L and S refer to the large and small patches, respectively (see Fig. S3, ESI†). The smaller of the patches, θ_s^*, has a size comparable to that obtained for the kagome lattice, as expected based on the coordination of the kagome and snub square lattices. This (θ_s^*, λ^*) combination is well within the region where a maximum of two-bonds-per-patch are allowed in 2D. The size of the larger patch, however, is larger than the four-bond-per-patch lower limit ($\approx 65°$) at $\lambda^* = 1.10$ (see Fig. S3, ESI†).

Fig. 6 summarizes the results from a self-assembly simulation with the optimized parameters for snub square assembly. Fig. 6 shows a configuration from the simulation, where we observe a high yield of $\Upsilon \approx 94\%$ (red line in Fig. 6b). The RDF of the self-assembled crystal, shown in blue in Fig. 6c, is in excellent agreement with the RDF of the ideal crystal (dashed black lines). As in Fig. 3 and 5, the radial axis is normalized by the location of the first peak, which is $r_0 \approx 1.0438$ for the assembled crystal. Following the analysis of the kagome and pyrochlore case studies, it is clear that this r_0 is commensurate with the target crystal density of $\phi_{\text{target}} = 0.59$.

It is counterintuitive that the size of the larger patch is above the four-bond-per-patch lower limit, especially when considering the fact that the small patches from this particular optimization, as well as

the small patches in the optimized model for kagome, are well within the range where a maximum of two bonds per patch are allowed. Despite this fact, we do not observe any large patches accommodating more than three bonded neighbors in any of the assembly simulations of this model, which would yield the coordination of the close-packed crystal structure that is clearly incompatible with the snub square crystal structure. To test the effect of the coverage of the larger patch on assembly, we performed additional self-assembly simulations with θ_L values in the range $60° \leq \theta_L \leq 66°$, *i.e.*, which spans values where a maximum of three or four bonds-per-patch are allowed. We observe that a pure snub square lattice is only obtained when θ_L is close to or slightly larger than the minimum aperture required to accommodate four bonds per patch (see ESI†), with the highest quality crystal obtained from simulations with the optimized parameters mentioned above. This result is analogous to a previous result using digital alchemy to optimize an isotropic Lennard-Jones–Gauss potential to stabilize a square lattice, where the thermodynamically optimal value did not correspond to the naïve ansatz obtained from pattern registration between the RDF and the potential.[45] This counterintuitive result illustrates that, in some instances, successful self-assembly can be promoted with parameters that do not correspond to a naïve geometrical ansatz, and that the digital alchemy inverse design framework is capable of finding such nontrivial solutions.

4. Conclusions

In this work, we extended the digital alchemy framework for the inverse design of particles with anisotropic energetic interactions.

To avoid trivial solutions (such as infinitely strong interactions that match the valency of the target structure), we constrained the alchemical variables (*i.e.*, the parameters of the interaction model) to the surface defined by a constant second virial coefficient (b_2) of the potential. This choice of constraint is motivated by the crystallization slot concept in proteins, whereby a relatively narrow range of b_2 promotes crystallization. Although b_2 values within this slot may be insufficient to promote successful crystallization in some cases due to kinetic limitations, the concept remains a useful guide for screening the high-dimensional space of parameters that influence crystal yield. Here, the use of the b_2 constraint led to successful design of patchy particles that self-assemble colloidal crystals in all three example cases studied.

We showed how this approach can be used to design symmetric triblock Janus spheres modeled with the Kern–Frenkel potential to self-assemble technologically relevant structures; specifically, we designed symmetric triblock Janus spheres to self-assemble a kagome lattice in 2D and the pyrochlore lattice in 3D. In both cases, we obtained optimal potential parameters α^* that are in good agreement with previous studies of the equilibrium phase diagram of the Kern–Frenkel potential. In general, we observe that both the aperture angle θ^* as well as the interaction range λ^* are relatively unaffected by the value of the b_2 constraint. The former is most strongly correlated with the valency of the target structure, where the surface coverage of the patch is dictated by how many bonds the patch must accommodate in the target structure. The latter is most strongly correlated with the density of the target crystal phase, which is unsurprising since the range of interaction ultimately determines the density of the crystal phase; this fact allows tuning of the lattice spacing of the self-assembled crystal structures.

To demonstrate the broad applicability of our method, we relaxed the symmetric patch condition and designed the first Kern–Frenkel model with asymmetric patches that successfully self-assembles the snub square lattice. The aperture angle of the smaller patch lies within the two bonds-per-patch limits, as expected by geometrical considerations alone. However, the larger patch is slightly above the four-bond-per-patch lower limit, despite the fact that the coordination of the crystal structure only requires three bonds per patch for the larger patch. This result highlights how our method yields results that are not easily predicted based on intuition and geometric considerations.

Future work will be aimed at extending our methodology to more general patchy particle potentials, including those that do not have a closed-form expression for b_2. We do not anticipate the lack of a closed-form expression for b_2 being a limitation as there are many available numerical methods to efficiently and accurately compute b_2 given its relevance in predicting thermodynamic properties. One particularly exciting future direction is the design of patchy particles with anisotropic shapes, as opposed to the spherical shapes used in the present work. Such work will enable the exploration of a design space with more anisotropy dimensions[15] than current methods allow and therefore represents an important step in particle design whereby energetic patchiness and entropic (shape) patchiness[88] can be tuned simultaneously to offer more precise control over self-assembling systems.

Finally, we again note that the digital alchemy framework, in its current form, finds values of the alchemical variables that minimize the free energy of the target structure at the target state point. Subsequent self-assembly from a fluid phase is not guaranteed because the free energy of the fluid phase at the target state point relative to the free energy of the crystal is not considered. Additionally, the free energies of polymorphs are not considered, and competing polymorphs may lower the assembly yield of the target lattice as we observed for the case of pyrochlore in the current work. We expect that additional alchemical degrees of freedom (*e.g.*, the shape of the patches) or further modifications to the alchemical inverse design framework (*e.g.*, incorporation of negative design strategies[37,44,79]) will help resolve these issues; such considerations are the subject of future work. Regardless, digital alchemy has proven a useful and reliable approach to patchy particle design.

Conflicts of interest

There are no conflicts to declare.

Acknowledgements

Notes and references

1 A. B. Pawar and I. Kretzschmar, *Macromol. Rapid Commun.*, 2010, **31**, 150–168.
2 G. Agrawal and R. Agrawal, *ACS Appl. Nano Mater.*, 2019, **2**, 1738–1757.
3 S. Ravaine and E. Duguet, *Curr. Opin. Colloid Interface Sci.*, 2017, **30**, 45–53.
4 W. Li, H. Palis, R. Merindol, J. Majimel, S. Ravaine and E. Duguet, *Chem. Soc. Rev.*, 2020, **49**, 1955–1976.
5 Q. Chen, S. C. Bae and S. Granick, *Nature*, 2011, **469**, 381–384.
6 F. Romano and F. Sciortino, *Soft Matter*, 2011, 7, 5799–5804.
7 X. Mao, Q. Chen and S. Granick, *Nat. Mater.*, 2013, **12**, 217–222.
8 D. Z. Rocklin and X. Mao, *Soft Matter*, 2014, **10**, 7569–7576.
9 W. D. Piñeros, M. Baldea and T. M. Truskett, *J. Chem. Phys.*, 2016, **145**, 054901.
10 W. D. Piñeros and T. M. Truskett, *J. Chem. Phys.*, 2017, **146**, 144501.
11 W. D. Piñeros, B. A. Lindquist, R. B. Jadrich and T. M. Truskett, *J. Chem. Phys.*, 2018, **148**, 104509.

12 C. S. Adorf, J. Antonaglia, J. Dshemuchadse and S. C. Glotzer, *J. Chem. Phys.*, 2018, **149**, 204102.

13 A. Kim, T. Vo, H. An, P. Banerjee, L. Yao, S. Zhou, C. Kim, D. J. Milliron, S. C. Glotzer and Q. Chen, *Nat. Commun.*, 2022, **13**, 1–14.

14 A. Kim, L. Yao, F. Kalutantirige, S. Zhou and Q. Chen, *Self-Assembly of Nanostructures and Patchy Nanoparticles*, IntechOpen, 2020.

15 S. C. Glotzer and M. J. Solomon, *Nat. Mater.*, 2007, **6**, 557–562.

16 G. M. Coli, E. Boattini, L. Filion and M. Dijkstra, *Sci. Adv.*, 2022, **8**, eabj6731.

17 M. Rechtsman, F. Stillinger and S. Torquato, *Phys. Rev. E: Stat., Nonlinear, Soft Matter Phys.*, 2006, **73**, 011406.

18 S. Torquato, *Soft Matter*, 2009, **5**, 1157–1173.

19 M. C. Rechtsman, F. H. Stillinger and S. Torquato, *Phys. Rev. Lett.*, 2005, **95**, 228301.

20 A. Jain, J. R. Errington and T. M. Truskett, *Soft Matter*, 2013, **9**, 3866–3870.

21 G. Zhang, F. H. Stillinger and S. Torquato, *Phys. Rev. E: Stat., Nonlinear, Soft Matter Phys.*, 2013, **88**, 042309.

22 E. Marcotte, F. H. Stillinger and S. Torquato, *Soft Matter*, 2011, **7**, 2332–2335.

23 A. Jain, J. R. Errington and T. M. Truskett, *Phys. Rev. X*, 2014, **4**, 031049.

24 W. D. Piñeros, M. Baldea and T. M. Truskett, *J. Chem. Phys.*, 2016, **144**, 084502.

25 É. Marcotte, F. H. Stillinger and S. Torquato, *J. Chem. Phys.*, 2013, **138**, 061101.

26 R. Jadrich, B. Lindquist and T. Truskett, *J. Chem. Phys.*, 2017, **146**, 184103.

27 B. A. Lindquist, *J. Chem. Phys.*, 2021, **154**, 174907.

28 E. Edlund, O. Lindgren and M. N. Jacobi, *Phys. Rev. Lett.*, 2011, **107**, 085503.

29 H. Cohn and A. Kumar, *Proc. Natl. Acad. Sci. U. S. A.*, 2009, **106**, 9570–9575.

30 R. Kumar, G. M. Coli, M. Dijkstra and S. Sastry, *J. Chem. Phys.*, 2019, **151**, 084109.

31 D. Banerjee, B. A. Lindquist, R. B. Jadrich and T. M. Truskett, *J. Chem. Phys.*, 2019, **150**, 124903.

32 B. A. Lindquist, R. B. Jadrich and T. M. Truskett, *J. Chem. Phys.*, 2016, **145**, 111101.

33 P. Zhou, J. C. Proctor, G. van Anders and S. C. Glotzer, *Mol. Phys.*, 2019, **117**, 3968–3980.

34 W. D. Piñeros, R. B. Jadrich and T. M. Truskett, *AIP Adv.*, 2017, **7**, 115307.

35 F. A. Escobedo, *J. Chem. Phys.*, 2017, **147**, 214501.

36 D. Chen, G. Zhang and S. Torquato, *J. Phys. Chem. B*, 2018, **122**, 8462–8468.

37 F. Romano, J. Russo, L. Kroc and P. Šulc, *Phys. Rev. Lett.*, 2020, **125**, 118003.

38 U. T. Lieu and N. Yoshinaga, *J. Chem. Phys.*, 2022, **156**, 054901.

39 Y. Ma and A. L. Ferguson, *Soft Matter*, 2019, **15**, 8808–8826.

40 Y. Ma, J. C. Aulicino and A. L. Ferguson, *J. Phys. Chem. B*, 2021, **125**, 2398–2410.

41 F. Romano and F. Sciortino, *Nat. Commun.*, 2012, **3**, 1–6.

42 E. G. Noya, C. K. Wong, P. Llombart and J. P. Doye, *Nature*, 2021, **596**, 367–371.

43 D. F. Tracey, E. G. Noya and J. P. Doye, *J. Chem. Phys.*, 2021, **154**, 194505.

44 J. Russo, F. Romano, L. Kroc, F. Sciortino, L. Rovigatti and P. Šulc, *J. Phys.: Condens. Matter*, 2022, **34**, 354002.

45 G. van Anders, D. Klotsa, A. S. Karas, P. M. Dodd and S. C. Glotzer, *ACS Nano*, 2015, **9**, 9542–9553.

46 Y. Geng, G. van Anders and S. C. Glotzer, arXiv, 2018, preprint arXiv:1801.06219.

47 R. K. Cersonsky, G. van Anders, P. M. Dodd and S. C. Glotzer, *Proc. Natl. Acad. Sci. U. S. A.*, 2018, **115**, 1439–1444.

48 C. X. Du, G. van Anders, J. Dshemuchadse, P. M. Dodd and S. C. Glotzer, *Mol. Simul.*, 2020, **46**, 1037–1044.

49 Y. Geng, G. van Anders, P. M. Dodd, J. Dshemuchadse and S. C. Glotzer, *Sci. Adv.*, 2019, **5**, eaaw0514.

50 J. W. Morgan and S. C. Glotzer, *J. Chem. Phys.*, 2020, **152**, 014106.

51 P. Zhou and S. C. Glotzer, *Eur. Phys. J. B*, 2021, **94**, 1–10.

52 A. George and W. W. Wilson, *Acta Crystallogr., Sect. D: Biol. Crystallogr.*, 1994, **50**, 361–365.

53 A. Ben-Naim, *Statistical thermodynamics for chemists and biochemists*, Springer Science & Business Media, 1992.

54 G. Vliegenthart and H. N. Lekkerkerker, *J. Chem. Phys.*, 2000, **112**, 5364–5369.

55 M. G. Noro and D. Frenkel, *J. Chem. Phys.*, 2000, **113**, 2941–2944.

56 F. Platten, N. E. Valadez-Pérez, R. Castañeda-Priego and S. U. Egelhaaf, *J. Chem. Phys.*, 2015, **142**, 05B602_1.

57 D. S. Tomar, S. Kumar, S. K. Singh, S. Goswami and L. Li, *MAbs*, 2016, 216–228.

58 C. Haas and J. Drenth, *J. Phys. Chem. B*, 1998, **102**, 4226–4232.

59 C. Hitscherich Jr, M. Allaman, J. Wiencek, J. Kaplan and P. J. Loll, *Protein Sci.*, 2000, **9**, 1559–1566.

60 F. Bonnete and D. Vivares, *Acta Crystallogr., Sect. D: Biol. Crystallogr.*, 2002, **58**, 1571–1575.

61 T. Ahamed, B. N. Esteban, M. Ottens, G. W. Van Dedem, L. A. Van der Wielen, M. A. Bisschops, A. Lee, C. Pham and J. Thömmes, *Biophys. J.*, 2007, **93**, 610–619.

62 T. K. Haxton and S. Whitelam, *Soft Matter*, 2012, **8**, 3558–3562.

63 M. Kastelic, Y. V. Kalyuzhnyi, B. Hribar-Lee, K. A. Dill and V. Vlachy, *Proc. Natl. Acad. Sci. U. S. A.*, 2015, **112**, 6766–6770.

64 D. Frenkel, *Phys. A*, 1999, **263**, 26–38.

65 J. Blouwolff and S. Fraden, *J. Cryst. Grow.*, 2007, **303**, 546–553.

66 W. W. Wilson and L. J. DeLucas, *Acta Crystallogr., Sect. F: Struct. Biol. Commun.*, 2014, **70**, 543–554.

67 Q. Chen, E. Diesel, J. K. Whitmer, S. C. Bae, E. Luijten and S. Granick, *J. Am. Chem. Soc.*, 2011, **133**, 7725–7727.

68 N. Kern and D. Frenkel, *J. Chem. Phys.*, 2003, **118**, 9882–9889.

69 J. A. Anderson, M. E. Irrgang and S. C. Glotzer, *Comput. Phys. Commun.*, 2016, **204**, 21–30.

70 J. A. Anderson, J. Glaser and S. C. Glotzer, *Comput. Mater. Sci.*, 2020, **173**, 109363.

71 R. Hołyst, D. Plewczyński, A. Aksimentiev and K. Burdzy, *Phys. Rev. E: Stat., Nonlinear, Soft Matter Phys.*, 1999, **60**, 302.

72 V. Ramasubramani, B. D. Dice, E. S. Harper, M. P. Spellings, J. A. Anderson and S. C. Glotzer, *Comput. Phys. Commun.*, 2020, **254**, 107275.

73 E. G. Teich, G. van Anders and S. C. Glotzer, *Nat. Commun.*, 2019, **10**, 1–10.

74 W. F. Reinhart and A. Z. Panagiotopoulos, *J. Chem. Phys.*, 2016, **145**, 094505.

75 P. J. Steinhardt, D. R. Nelson and M. Ronchetti, *Phys. Rev. B: Condens. Matter Mater. Phys.*, 1983, **28**, 784.

76 W. Lechner and C. Dellago, *J. Chem. Phys.*, 2008, **129**, 114707.

77 N. A. Mahynski, L. Rovigatti, C. N. Likos and A. Z. Panagiotopoulos, *ACS Nano*, 2016, **10**, 5459–5467.

78 A. B. Rao, J. Shaw, A. Neophytou, D. Morphew, F. Sciortino, R. L. Johnston and D. Chakrabarti, *ACS Nano*, 2020, **14**, 5348–5359.

79 J. P. Doye, A. A. Louis, I.-C. Lin, L. R. Allen, E. G. Noya, A. W. Wilber, H. C. Kok and R. Lyus, *Phys. Chem. Chem. Phys.*, 2007, **9**, 2197–2205.

80 Z. Zhang, A. S. Keys, T. Chen and S. C. Glotzer, *Langmuir*, 2005, **21**, 11547–11551.

81 M. Antlanger, G. Doppelbauer and G. Kahl, *J. Phys.: Condens. Matter*, 2011, **23**, 404206.

82 J. A. Millan, D. Ortiz, G. Van Anders and S. C. Glotzer, *ACS Nano*, 2014, **8**, 2918–2928.

83 D. Salgado-Blanco and C. I. Mendoza, *Soft Matter*, 2015, **11**, 889–897.

84 C. Zhang, M. Su, Y. He, X. Zhao, P.-A. Fang, A. E. Ribbe, W. Jiang and C. Mao, *Proc. Natl. Acad. Sci. U. S. A.*, 2008, **105**, 10665–10669.

85 D. Écija, J. I. Urgel, A. C. Papageorgiou, S. Joshi, W. Auwärter, A. P. Seitsonen, S. Klyatskaya, M. Ruben, S. Fischer and S. Vijayaraghavan, *et al.*, *Proc. Natl. Acad. Sci. U. S. A.*, 2013, **110**, 6678–6681.

86 L. Liu, Z. Li, Y. Li and C. Mao, *J. Am. Chem. Soc.*, 2019, **141**, 4248–4251.

87 C. Nürnberger, H. Lu, X. Zeng, F. Liu, G. Ungar, H. Hahn, H. Lang, M. Prehm and C. Tschierske, *Chem. Commun.*, 2019, **55**, 4154–4157.

88 G. van Anders, D. Klotsa, N. K. Ahmed, M. Engel and S. C. Glotzer, *Proc. Natl. Acad. Sci. U. S. A.*, 2014, **111**, E4812–E4821.

Supplementary Information for "Inverse design of triblock Janus spheres for self-assembly of complex structures in the crystallization slot *via* digital alchemy"

Luis Y. Rivera-Rivera,[a‡] Timothy C. Moore,[a‡] and Sharon C. Glotzer[*ab]

b_2-constrained alchemy with independent patch aperture fluctuations

Figure S1 shows the evolution of the alchemical variables during alchemical simulations where the aperture angles of the two patches (θ_1 and θ_2) are allowed to fluctuate independently of one another. For the system biased towards the kagome lattice (Figure S1a–d), θ_1 and θ_2 converge to the same value (approximately 37°) for all successful optimizations, reflecting the symmetry of the valence of each particle in the kagome lattice. In contrast, for the case of snub square, θ_1 and θ_2 converge to different values, approximately 67° and 38°. This difference reflects the asymmetric valence around each particle in the snub square lattice.
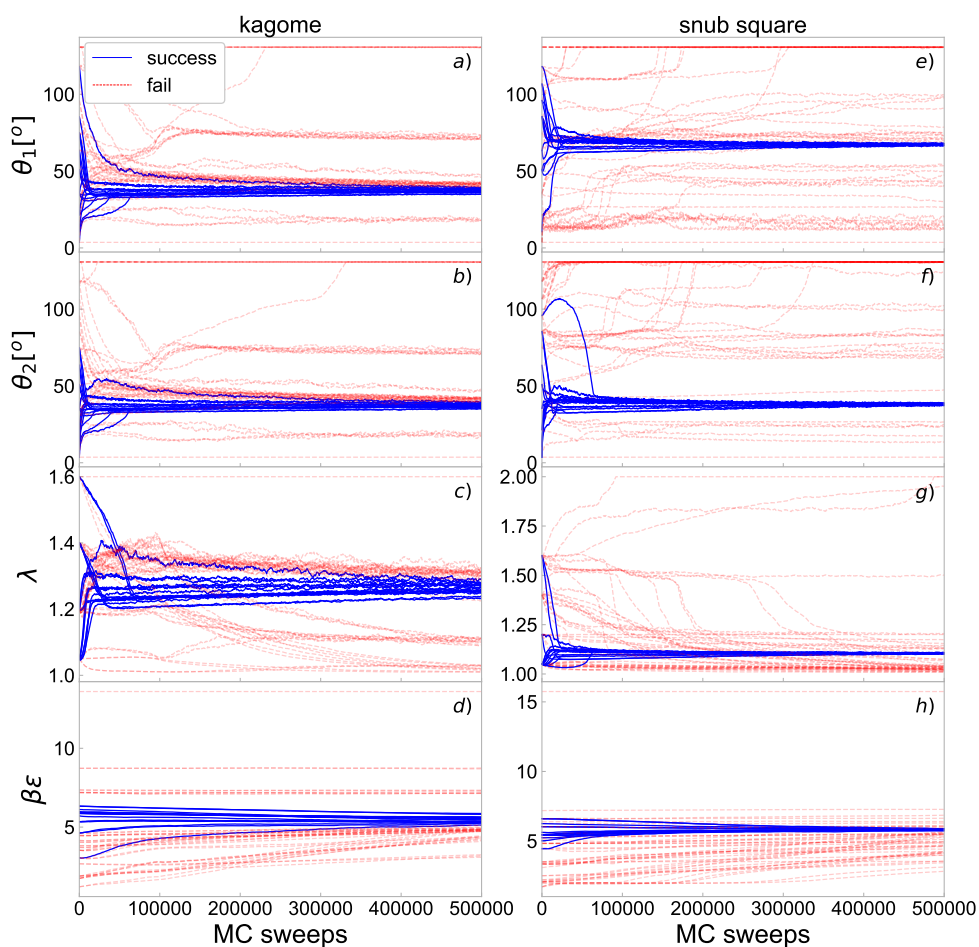

Fig. S1 Alchemical variables as a function of the MC sweeps when the equal-size aperture angle constraint is relaxed for kagome (a–d) at $(b_2, \phi_{\text{target}}) = (-9, 0.5)$, and snub square (e–h) at $(b_2, \phi_{\text{target}}) = (-19, 0.59)$.

[a] *Department of Chemical Engineering, University of Michigan, Ann Arbor, MI, USA.*

[b] *Biointerfaces Institute, University of Michigan, Ann Arbor, MI, USA.*

[‡] *These authors contributed equally to this work.*

Snub square design: pattern registration analysis

Figure S2 shows the final snapshot of self-assembly simulations performed with $\theta_L = 60°, 62°, 64°$ and $66°$, while keeping the smaller patch aperture angle fixed at $\theta_S = 38°$. The first three values are large enough to accommodate a maximum of three bonds per patch while the last one is slightly larger than the minimum required to accommodate four bonds per patch. From these pattern registration considerations alone, we would expect to observe the formation of a high quality snub-square lattice with the first three values of θ_L. However, this is not the case. Instead, we observe the formation of kagome/twisted kagome at $\theta_L = 60°$. Slightly increasing the aperture angle to $\theta_L = 62°$ results in a snub square/twisted kagome coexistence. Finally, we observe the assembly of a pure snub square lattice only when $\theta_L \in \{64°, 66°\}$, that is, when θ_L is close to or slightly larger than the minimum aperture required to accommodate a maximum of four bonds per patch. We also note that the snub square lattice obtained from the systems with $\theta_L \in \{64°, 66°\}$ exhibits a considerable number of defects, whereas the lattice obtained with the optimized parameters is relatively defect free (Figure 6, main text).
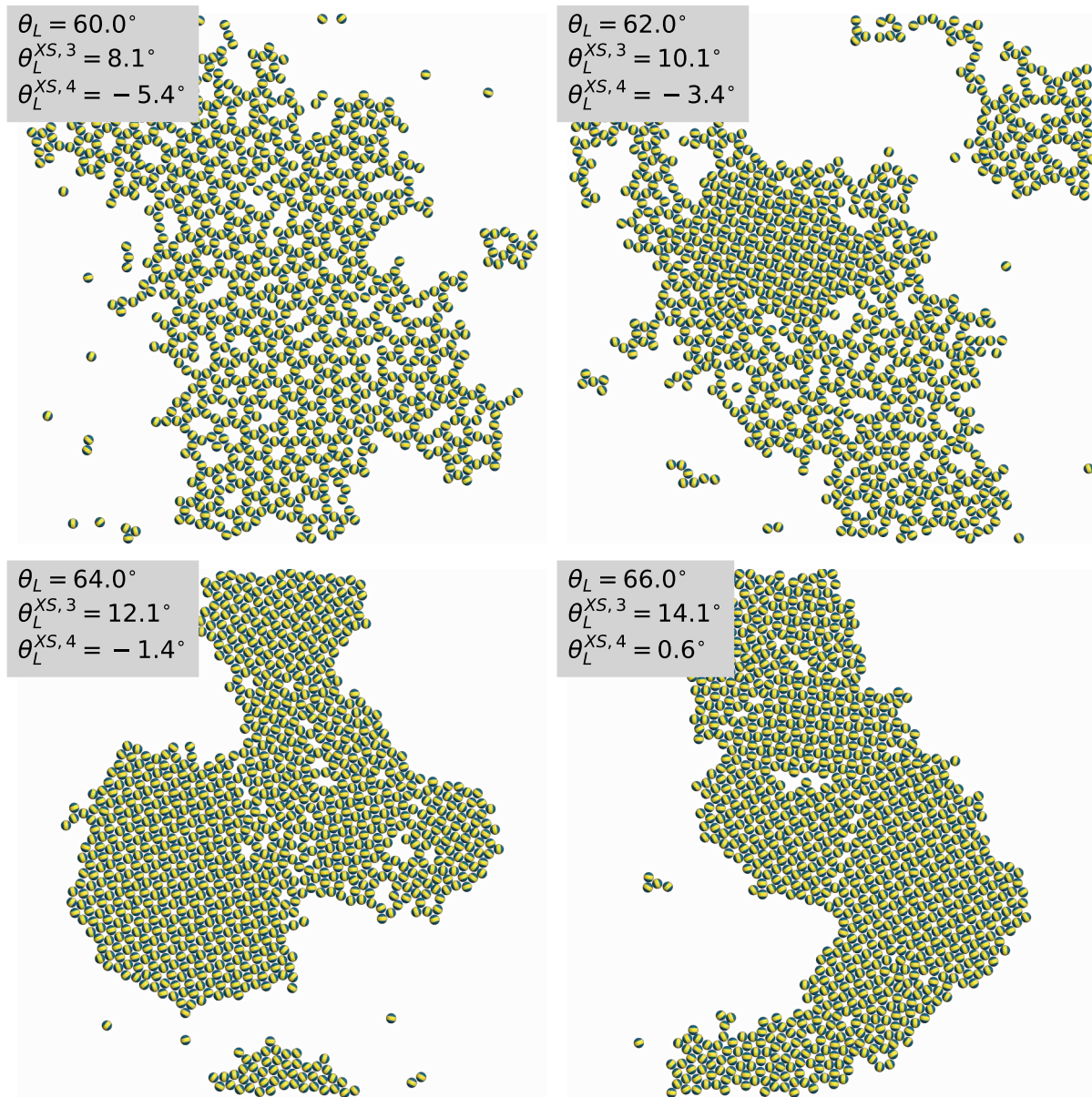

Fig. S2 Final snapshot of self-assembly simulations at $\theta_L = 60°, 62°, 64°$ and $66°$ with fixed $\theta_S = 38°$. Here, the upper left symbol θ_L^{XS} denotes how much larger θ_L is above the minimum for three-bonds-per-patch ($\approx 52°$) for $\lambda = 1.10$.

Bonds-per-patch analysis

The maximum number of bonds a given patch can form to other bonds is dictated by the aperture angle θ and patchy interaction range λ. The range of λ and θ values where patches can form at most n bonds is given by

$$C_{\min}^{(n)} \leq \lambda \sin\theta < C_{\max}^{(n)}.$$

In two-dimensions, $(C_{\min}^{(n)}, C_{\max}^{(n)})$ pairs are given by $(0, 1/2)$, $(1/2, 1/\sqrt{3})$, and $(1/\sqrt{3}, 1/\sqrt{2})$ for $n = 1$, 2, and 3, respectively. In 3D, these pairs are given by $(0, 1/2)$, $(1/2, \sqrt{3}/2)$, and $(\sqrt{3}/2, 1)$ for $n = 1$, 2, and 3, respectively.
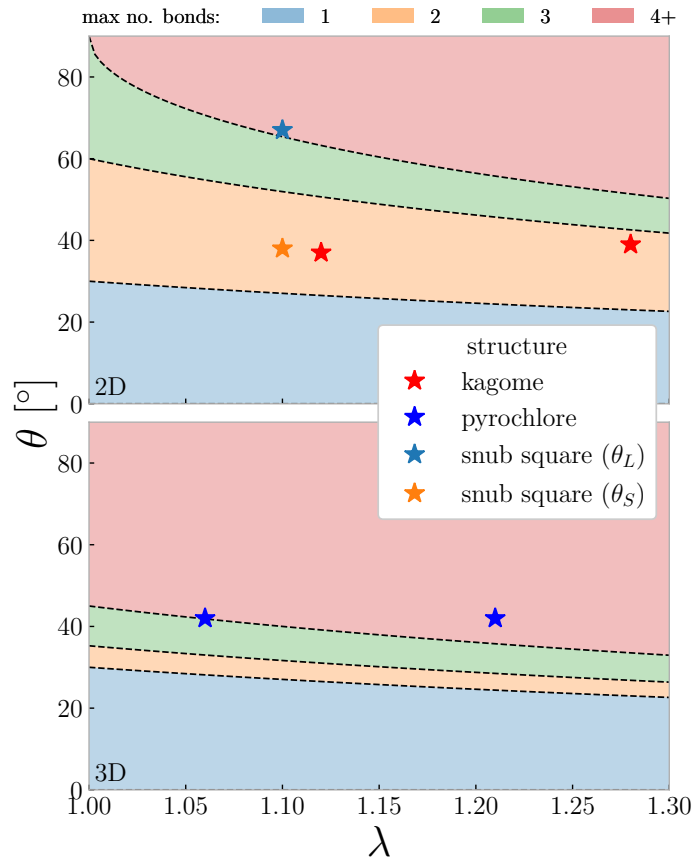

Fig. S3 The range of patch aperture angles θ that allow a maximum of 1, 2, 3, and 4 bonds per patch as a function of λ for 2D (top) and 3D (bottom). Optimized parameters for selected structures shown as colored stars.